# Morpho-Structural Characterization and Electrophoretic Deposition of Xonotlite Obtained by a Hydrothermal Method

***Jelena Čović; Ivana Jovanović; Aleksandra Zarubica; Aleksandar Bojić; Marjan Ranđelović****+

*The University of Niš, Faculty of Sciences and Mathematics, Department of Chemistry, 33 Višegradska St., 18000 Niš, SERBIA*

**ABSTRACT:** *In this research, xonotlite was synthesized by a hydrothermal method in the Si-Ca-Na-$H_2O$ system. Detailed structural characterization by using the XRD technique revealed that the obtained material contains a small quantity of wollastonite (up to 3 %) as an impurity. Calcination of the obtained sample at 900 ˚C has resulted in a complete transformation of xonotlite to wollastonite which was detected as only a crystal phase. Crystallite size and lattice strain of all crystal phases were calculated using Scherrer and Williamson-Hall method. SEM observation of xonotlite morphology revealed tiny needle-like crystals joined together forming dendritic or globular aggregates. Optimal conditions for electrophoretic deposition of xonotlite on 304-type stainless steel have been achieved by appropriate selection of electric field strengths, dispersing medium, and dispersants. Stable suspension of the material was obtained using isopropanol containing 1 % water as dispersing medium and Ca-nitrate as a charging additive. Native layers of xonotlite have a very smooth morphology, while after calcination, the appearance of small cracks in the coating can be observed but the adhesion strength of the coatings to the substrate is improved.*

**KEYWORDS:** *Xonotlite; Wollastonite; Hydrothermal synthesis; Electrophoretic deposition.*

## INTRODUCTION

Xonotlite is a fibrous calcium silicate hydrate (C-S-H) whose chemical composition is $Ca_6Si_6O_{17}(OH)_2$. The mineral xonotlite commonly appears in nature as needle-like crystals and as flaky fibrous radiating bundles and rosettes, together with metamorphic deposits within limestones, serpentinites, and metavolcanic rocks [1,2].

The structure of xonotlite consists of Ca-O-polyhedral layers and $[Si_6O_{17}]$-double silicate chains. There are two types of Ca-polyhedra, 1/3 of which are 6-fold coordinated, and 2/3 being 7-fold coordinated. The $CaO_6$-octahedra and $CaO_7$-polyhedra in seven-fold coordination are both edge-sharing to form infinite chains in the b-direction. The double silicate chains $[Si_6O_{17}]$ are linked via undulating sheets of edge-sharing Ca-polyhedra stacked along the c-direction [3]. Considering its chemical composition, xonotlite is closely related to that of another chain silicate

* *To whom correspondence should be addressed.*
*+ E-mail: hemija@gmail.com*
*1021-9986/2022/6/1932-1941 9/$/5.09*

mineral-wollastonite, $CaSiO_3$. Consequently, upon calcination/dehydration, xonotlite can be easily transformed into wollastonite [3].

The porosity is the main characteristic of xonotlite which is the basis for its industrial applications. Nowadays, xonotlite is widely used as a thermally insulating material and for the removal and recovery of phosphate from an aqueous solution. Moreover, it is often found as a component in types of cement, and reinforcement in organic polymers; it has also been used for refractory boards, fireproof materials, ceiling boards, microporous materials, architectural boards, and lightweight boards, material for the removal of organic polyelectrolytes and their metal complexes by adsorption, for heavy metal uptake, etc. [4].

The preparation of calcium silicate hydrate fibers, especially xonotlite has been attracting attention in recent years [5-9]. Previous studies suggested that various biomaterials containing calcium silicate components such as bioglass [10,11], $CaSiO_3$ [12], and $Ca_2SiO_4$ ceramics [13,14] were bioactive and could induce the formation of the bonelike apatite in the Simulated Body Fluid (SBF).

There are a lot of techniques for the application of coatings onto metallic substrates such as physical vapor deposition, chemical vapor deposition, electrochemical vapor deposition methods, plasma technologies, spraying techniques, dip-coating, screen-printing, slip-casting, etc. Among them, ElectroPhoretic Deposition (EPD) stands out as a particularly attractive technique because of its advantages of short formation time, needs simple apparatus, little restriction of the shape of the substrate, and no requirement for binder burnout as the green coating contains few or no organics. Compared to other advanced techniques, the EPD process can be made on flat, cylindrical, or any other shaped substrate with only minor changes in electrode design and positioning [15].

The main goal of this study was to present an easy one-pot synthesis of xonotlite from simple and economical precursors as well as to determine electrophoretic parameters for its successful deposition onto stainless steel substrates (S.S. substrates). Xonotlite was prepared from the solution of sodium-metasilicate and calcium-nitrate by hydrothermal treatment and deposited onto an S.S substrate. The calcination of obtaining coating was carried out at 900 °C to achieve stability of coatings, adherence to the substrate, and phase transformations of xonotlite do wollastonite crystal phase. Detailed and structural characterizations of powders and coatings were completed to study the surface smoothness, shapes, and size of particles as well as crystal phases present in the samples. The research highlights also optimal conditions for the electrophoretic deposition of xonotlite onto a cathode made of stainless steel.

## EXPERIMENTAL SECTION

### *Xonotlite synthesis*

The amount of 3.54 g $Ca(NO_3)_2 \cdot 4H_2O$ was dissolved in 35 mL of deionized water and the solution was stirred for 5 min using a magnetic stirrer. In a separate beaker, 3.18 g $Na_2SiO_3 \cdot 5H_2O$ was dissolved in another 35 mL of deionized water and then dropped into $Ca(NO_3)_2$ solution to obtain a milky-white suspension. The suspension was stirred for 30 min to ensure that the particles are well mixed and completely dispersed into the liquid. The suspension was then transferred into stainless steel autoclave, and heated at 220 ˚C for 240 min at autogenous pressure of 19 bar, followed by cooling to room temperature naturally. After the hydrothermal reaction, the obtained suspension was filtrated and washed with deionized water three times. The resultant powder was dried at 105 °C for 3 h.

### *Electrophoretic deposition*

To obtain a stable suspension of xonotlite, isopropanol containing 1% water was selected as dispersing phase, and $Ca^{2+}$ as an ionic dispersant was used. The dispersant was first added to a solution and then mixed for approximately 15 min to obtain a homogeneous charging medium. Subsequently, xonotlite nanoparticles were slowly added to the solution to obtain milky-white suspensions which had to undergo physical dispersion such as ultrasonic agitation of 30 min before deposition.

Electrophoretic deposition (EPD) was performed using a two-electrode Pyrex cell at a temperature of 25 °C. The working (substrate) electrode was the plate 304 stainless steel with a dimension of 78x25x0.4 mm, while the counter electrode was a titanium sheet. Before it was used as a substrate, the stainless steel plate had been initially washed using detergents, degreased with acetone and ultrasonication, and finally electrochemically etched in 0.5 M solution of oxalic acid with a constant current of 0.5 A. Only 40x25 mm of substrates were exposed to the deposition of xonotlite.

EPD was performed at three electric field strengths i) 14, ii) 28, and 43 V/cm for 5 min using a laboratory D.C. power supply (BK Instruments programmable DC power supply 1786B). The current density during EPD was recorded to be 1 mA/cm$^2$. Deposition mass was studied by weighing the substrate before and after EPD using a 0.1 mg accuracy balance (KERN ALS 220-4). EPD was performed once for field strengths of 14 and 28 V/cm and three times in a sequence for 43 V/cm with ultrasonication of suspension for 3 min between each EPD cycle to obtain the final uniformly coated substrate. After deposition of the third layer, the specimen was dried at room temperature and then calcined for 2 h at a temperature of 900 °C to obtain the wollastonite phase. The heating rate was 7.5 ˚C/min.

### *Characterization*

The microstructures of the powder samples and coatings on stainless steel substrates (S.S. substrates) were analyzed by Scanning Electron Microscopy (SEM) using a JEOL JSM-6610LV and a digital microscope Motic D-EL1. Structural characteristics of crystal phases were examined by X-ray diffraction, using a Siemens D500 diffractometer running with CuKα radiation.

Additional structural characterization of the powder samples was performed by Raman spectroscopy using a Raman Spectrometer (Renishaw inVia 2 Raman Microscope) equipped with a thermoelectric-cooled CCD detector. Samples were excited with a 532 nm laser system and focused on the samples through a microscope objective lens.

All IR absorption spectra were recorded in the wavenumber range of 400–4000 cm$^{-1}$ (transmission mode) using a Bomem spectrometer. The resolution used was 4 cm$^{-1}$ and the number of scans was 32.

### *Preparation of Simulated Body Fluid (SBF)*

Simulated Body Fluid (SBF) is a solution with an ion concentration nearly equal to those of human blood plasma. SBF can be used *in vitro* testing to study the biological activity of synthesized material. The consumption of calcium and phosphorus ions in the SBF solution is the result of the formation of apatite nuclei on the surface of biomaterials *in vitro* [16-18].

The preparation of the SBF solution requires the use of deionized water and chemical reagents of very high purity. The reagents are added one by one in the order given in Table 1 [19] with constant stirring and heating at 36.5-37 °C.

After adjusting the pH value to 7.4, the volumetric flask (100 mL of capacity) was filled with deionized water to the graduation mark. The prepared SBF solution was transferred to a polyethylene bottle and stored at a constant temperature until use. The amount of 0.25 g of calcined xonotlite in powder form was added to a 50 mL SBF solution and incubated for 7 days at a temperature of 37 °C to examine the potential formation of the apatite layer [19].

## RESULTS AND DISCUSSION

### *XRD analysis*

To identify the crystallinity and crystal phases of the as-synthesized xonotlite (xonotlite) and calcined xonotlite (wollastonite), X-Ray Diffraction (XRD) analysis was performed, and corresponding XRD patterns are shown in Fig. 1.

The main peaks of hydrothermally synthesized xonotlite can be found at 2θ = 11.40°, 22.97°, 26.77°, 34.84°, 38.97°, 41.05° in accordance with the reported JCPDS data (card no. 29-0379). However, there are also low-intensity peaks that suggest a small amount of wollastonite phase (up to 3%).

After calcination, XRD analysis confirmed the presence of wollastonite as a sole crystal phase. The wollastonite peaks (2θ) are as follows: 25.18°, 31.91°, 44.88°, 49.62°, 53.10°, 57.32°. No diffraction peaks arising from any impurity can be detected in the patterns of calcined samples confirming that the obtained product is only a crystal phase.

The average crystallite size ($D$) of the particles was determined from the XRD line broadening measurement using Scherrer's equation [20, 21](1):

$$D = \frac{K\lambda}{\beta_{hlk}\cos\theta} \quad (1)$$

where is: $K$ - shape factor (0.9), $\lambda$ - the *Cu* $K_{\alpha 1}$ radiation of wavelength (15.406 nm), $\beta_{hlk}$ - corrected Full Width at Half Maximum (FWHM) for instrumental broadening ($\beta_{hkl} = \beta_m - \beta_s$) in radians, whereas $\beta_m$ is observed half-width, and $\beta_s$ is half-width of the standard sample, and finally $\theta$ - the scattering angle.

***Table 1: Reagents for preparing SBF [19].***

| Order | Reagent | Amount |
|---|---|---|
| 1 | Deionized water | 40 mL |
| 2 | NaCl | 0,7996 g |
| 3 | $NaHCO_3$ | 0,035 g |
| 4 | KCl | 0,024 g |
| 5 | $K_2HPO_4$ | 0,0174 g |
| 6 | $MgCl_2$ x $6H_2O$ | 0,0305 g |
| 7 | HCl | 40 mL |
| 8 | $CaCl_2$ | 0,0278 g |
| 9 | $Na_2SO_4$ | 0,0071 g |
| 10 | Tris [$(CH_2OH)_3CNH_2$] | 0,6057 g |
| 11 | HCl | The appropriate amount for adjusting pH at 7.4 |

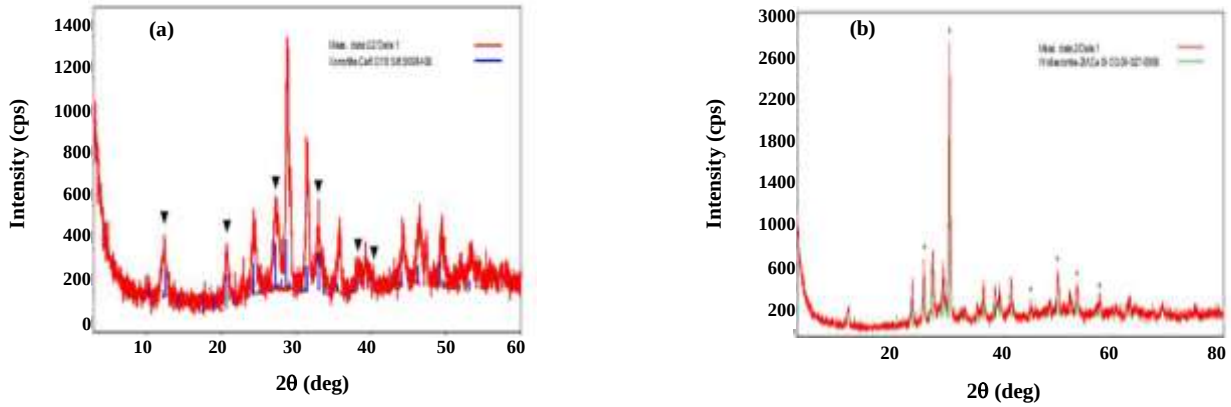


***Fig. 1: The X-ray diffraction patterns of xonotlite: a) before and b) after calcination at 900 °C.***

The calculated crystallite sizes for xonotlite and wollastonite in hydrothermally synthesized xonotlite samples are 9.58 and 2.48 nm, respectively. After calcination, the crystallite size of wollastonite was increased from 2.48 to 24.67 nm due to sintering at 900 °C. To understand the strain associated with the sample caused by lattice deformation, line-broadening analysis and calculations were carried out using the Williamson-Hall (W-H) method. Williamson and Hall proposed a good method for separation of strain and size effects on broadening by looking at the peak width as a function of diffracting angle [13,14], according to the equation:

$$\varepsilon = \frac{\beta_{hlk}}{4\tan\theta} \qquad (2)$$

Addition of the Scherrer equation and the volume-weighted average strain results in the following equations:

$$\beta_{hlk}\cos\theta = \frac{K\lambda}{D} + 4\varepsilon\sin\theta \qquad (3)$$

Where $\varepsilon$ is the microstrain. The strain value was obtained from the graph by the use of the W-H method.

A plot between 4 $sin\theta$ along the *x*-axis and $\beta_{hlk}cos\theta$ along the *y*-axis gives the slope of the curve to determine the strain ($\varepsilon$) associated with the lattice dislocations. It was found that strains arising from lattice dislocation for xonotlite and wollastonite which is present in synthesized samples up to 3%, were calculated from Equation (3) and their values are estimated to be 0.80 and 2.7, respectively. However, after calcination at 900 °C, the lattice strain

of the wollastonite crystal phase was decreased to 0.166 indicating a more ordered crystal structure. W-H analysis revealed a high value of microstrain in nanocrystals of xonotlite and wollastonite prior to calcination indicating a lot of crystal imperfections, dislocations, and distortions that significantly influenced peak broadening. For example, *Siddiqui et al.* have recently reported that the microstrain of synthesized CuO tetrapods is 0.00217 which is negligibly attributed to peak broadening [13].

***XRD analysis after interaction between calcined xonotlite (wollastonite) and SBF***

The product of the interaction between calcined xonotlite (wollastonite) and SBF is calcium hydroxyapatite. Fig. 2 presents XRD patterns after interaction between calcined xonotlite (wollastonite) and SBF. The characteristic peaks of hydroxyapatite ($Ca_{10}(PO_4)_6(OH)_2$) (2θ) can be found at: 25.87°, 31.78°, 46.71°, 49.46°, 53.14°, 57.12° in agreement with JCPDS no: 09-0432, while the peaks of wollastonite (2θ) was found at: 25.18°, 31.91°, 44.88°, 49.62°, 53.10°, 57.32°. By comparing the values of characteristic peaks of hydroxyapatite and the values of peaks of wollastonite [22], we can notice that these values coincide. However, in Fig. 2 can be seen that the peaks of hydroxyapatite (HA) are more intense and can be attributed to the HA phases.

***Raman spectroscopy***

The Raman spectra of xonotlite and calcined xonotlite (wollastonite) over the 100–1600 $cm^{-1}$ spectral range are shown in Figs. 3a and 3b, respectively. Xonotlite has chains of linked units of $Si_4O_{11}$ which show two bands at around 1040 and 1070 $cm^{-1}$ with an additional band at around 600 $cm^{-1}$ [23,24].

The Raman band at 995 $cm^{-1}$ is assigned to the SiO stretching vibrations of the $Si_4O_{11}$ and $Si_3O_{10}$, while the Raman band at 649 $cm^{-1}$ is attributed to the O-Si-O symmetric bending mode. The band at 502 $cm^{-1}$ is assigned to the O-Si-O bending modes of the $SiO_2$ units. In addition, bands at 410 and 318 $cm^{-1}$ are attributed to CaO stretching vibrations. Raman bands below 300 $cm^{-1}$ (e.g., 272, 225, 184, and 115 $cm^{-1}$) may simply be described as external vibration or lattice modes.

In Fig. 3 (b) three pronounced Raman bands at 1045, 972 and 856 $cm^{-1}$ can be observed. These three bands are assigned to SiO symmetric stretching vibrations of

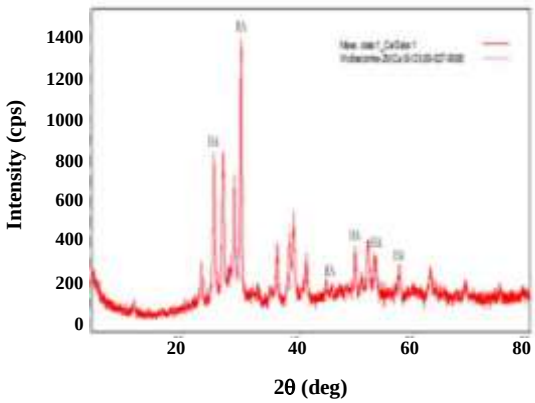


***Fig. 2: The X-ray diffraction patterns of calcined xonotlite sample (wollastonite) after interaction with SBF.***

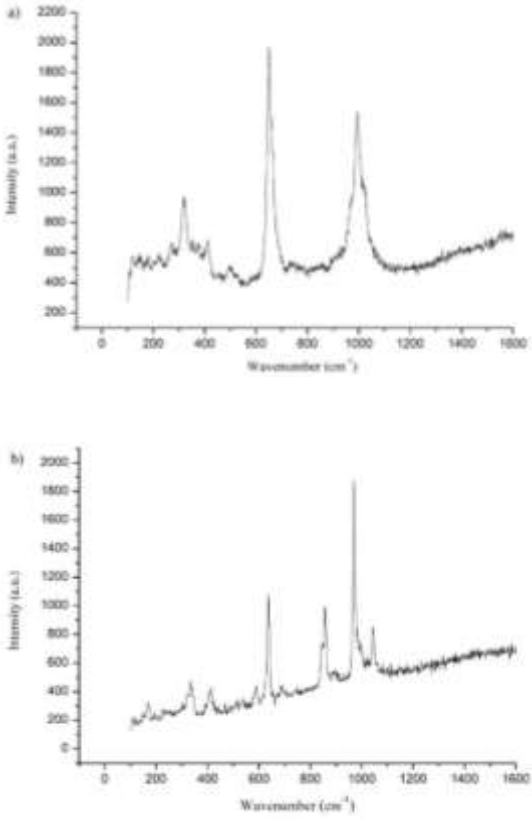

***Fig. 3: Raman spectrum of xonotlite and calcined xonotlite (wollastonite) over the 100–1600 $cm^{-1}$ spectral range. a) Raman spectrum of xonotlite; b) Raman spectrum of calcined xonotlite (wollastonite).***

wollastonite. Bands at 686 and 635 $cm^{-1}$ are assigned to O-Si-O bending vibration, while the band at 584 $cm^{-1}$ is assigned to O-Si-O bending modes of $SiO_2$ units. Two Raman bands at 410 and 336 $cm^{-1}$ are attributed to CaO stretching vibration,

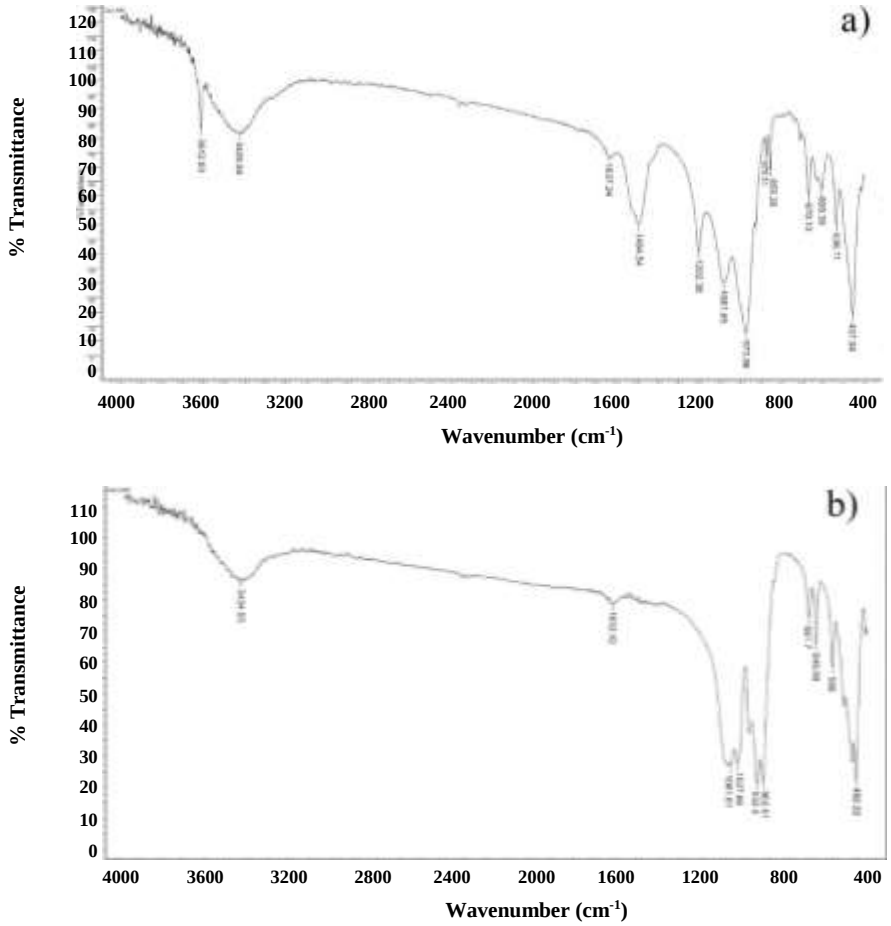


***Fig. 4: The infrared spectrum of a) xonotlite; b) wollastonite over the 400-4000 cm$^{-1}$ spectral range.***

while the band at 170 cm$^{-1}$ can be described as external vibration or lattice modes [24-26].

***FT-IR spectroscopy***

The infrared spectra of xonotlite and calcined xonotlite (wollastonite) in the 400-4000 cm$^{-1}$ range are displayed in Figs. 4a and 4b, respectively.

Xonotlite shows a very sharp spike at 3612 cm$^{-1}$, which is assigned to CaO–H stretching vibration while its bending mode is observed at 630 cm$^{-1}$.

The band at 3426 cm$^{-1}$ appeared due to water stretching vibration and the band at 1637 cm$^{-1}$ is attributed to water bending modes [27]. Water stretching vibration in the wollastonite spectrum is seen at 3434 cm$^{-1}$, while the band at 1632 cm$^{-1}$ is assigned to water bending vibrations. The absence of a band at 3612 cm$^{-1}$ in wollastonite spectra indicates that the dehydroxylation process occurred during calcination. The vibration at 1494 cm$^{-1}$ shows the presence of the carbonate group in xonotlite spectra which disappeared in the case wollastonite sample due to its thermal decomposition.

Xonotlite has a characteristic band at 1202 cm$^{-1}$ which occurs due to Si–O stretching of vibrations in $Q^3$ sites (silicate tetrahedra link two silicate chains). The infrared band at 1081 cm$^{-1}$ corresponds with the Si-O-Si asymmetric stretching vibration. Bands corresponding to Si–O stretching of Q2 sites appear at 980 cm$^{-1}$. The peak at 973 cm$^{-1}$ indicates the Si–O stretching of $Q^2$ sites, while bands at 670 and 609 cm$^{-1}$ are assigned to O-Si-O symmetric bending modes. Finally, peaks at 536 and 457 cm$^{-1}$ indicate deformation of the silicate network along with Ca-O stretching modes [28].

Calcined xonotlite (wollastonite) bands at 1061 and 1027 cm$^{-1}$ correspond with the Si-O-Si asymmetric stretching vibration. Bands at 932 and 902 cm$^{-1}$ are attributed to the O-Si-O asymmetric stretching vibration.

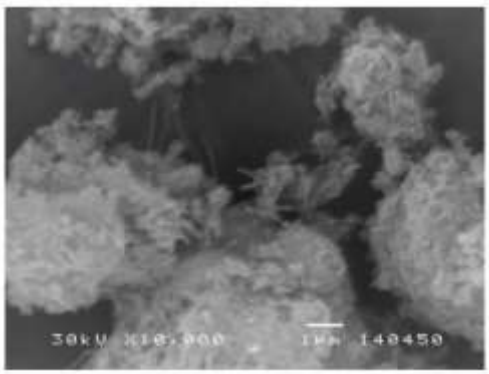

***Fig. 5: SEM micrograph of xonotlite.***

Two infrared bands at 681 and 646 $cm^{-1}$ are assigned to O-Si-O symmetric bending modes. Peaks at 566 and 452 $cm^{-1}$ show the presence of the Ca=O group and the deformation of the silicate network along with Ca-O stretching, respectively [25,26,29].

***SEM analysis***

Due to its structural characteristics, natural xonotlite materials tend to be produced as elongated crystals of about 1 μm. The SEM micrograph in Fig. 5 shows that the synthesized xonotlite mainly consists of tiny needle-like crystals joined together to form dendritic aggregates.

***Electrophoretic Deposition (EPD)***

Optimal characteristics of suspension, including conductivity, particle size, dielectric constant, and zeta potential were achieved by using isopropanol containing 1% of water as dispersing medium, finely ground xonotlite, and $Ca^{2+}$ as a charging additive.

Charge formation onto colloid particle surfaces can be ascribed to the dissociation of calcium nitrate in an isopropanol-water mixture providing positive ionic species due to the dissociation of $Ca(NO_3)_2$. As a result, increases in the suspension conductivity, electrophoretic mobility, and the zeta potential of the suspended particles were observed. The small amount of water present in the suspension induces minor electrolysis reactions after applying the electric field forming a $Ca(OH)_2$, which acts as a binder material n.

Consequently, the stability of suspension and adherence of the material to the substrate are increased. Moreover, such composition ensures optimal electrical conductivity of suspension which is measured to be 15.5 ± 1.5 μS/cm and zeta potential +31 mV.

The change of the deposit weight of xonotlite per surface area as a function of the applied voltage during EPD is shown in Fig. 6. As observed, the deposit weight increases as the voltage increases.

To obtain the final coating onto a selected substrate, electrophoretic deposition was successively repeated three times at a field strength of 43 V $cm^{-1}$. Multiple depositions were accompanied by drying at room temperature between each EPD cycle. The increase of deposit weight per surface area of substrate at each stage is shown in Fig. 7.

At a higher number of EPD cycles, the deposition rate decreases significantly. This may indicate that thicker coatings increase the electrical resistivity of the working electrode, which decreases the current flow and yield of deposition.

Fig. 8 shows the change in the deposit weight of xonotlite per surface area of the substrate of stainless steel as a function of the distance between the electrodes during EPD. As can be seen, the deposit weight of xonotlite increases with a decrease in the distance between the electrodes.

The optimal straight line was obtained by standard regression analysis using the linear least squares fitting technique. The slope of the straight line is 0.00113 and gives the weight of the deposited material of xonotlite on the electrode per unit of time. The slope of the straight line corresponds to the product $\mu ESC$ in Hamaker`s equation [30].

$$m = \mu EtSC_s \quad (4)$$

where is: $m$ - the mass of the deposit per unit area (g $cm^{-2}$), $\mu$ - the electrophoretic particle mobility ($cm^2$/V.s) in the electric field $E$ (V/cm), $t$ - deposition time (s), $S$ - the surface of the electrode, $C_s$ - the concentration of the solid phase in the suspension.

Linear dependence indicates that the process took place under conditions of constant current and constant concentration of the suspension. That has been confirmed by experimental observations during EPD [15]. During EPD, a constant current of 0,01 A is recorded at a constant voltage of 30 V. This is the simplest case of electrophoretic deposition and it can be explained as a consequence of a migration–coagulation mechanism.

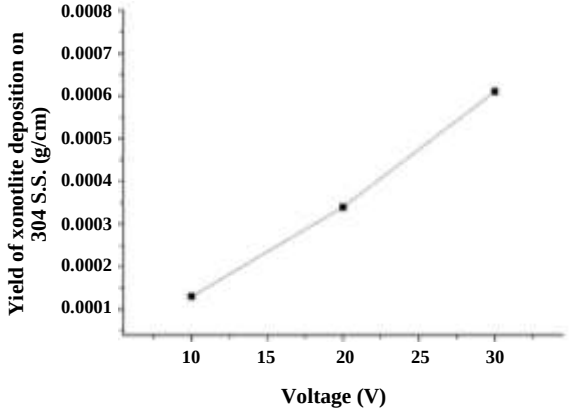


*Fig. 6: The deposit weight per surface area vs. applied electric field strength.*

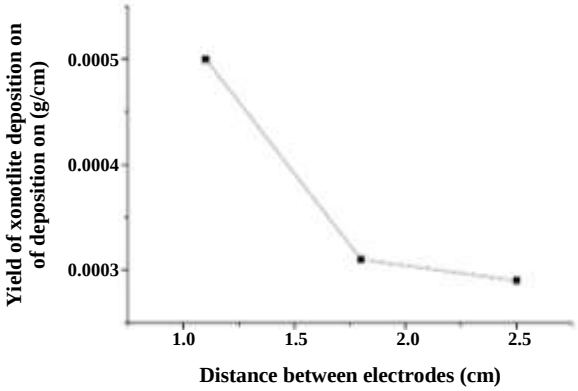


*Fig. 8: The deposit weight of xonotlite per surface area of the substrate of stainless steel as a function of the distance between the electrodes.*

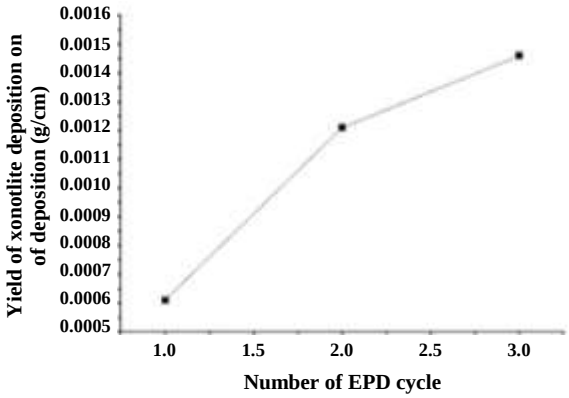


*Fig. 7: The yield of deposition of xonotlite per surface area of S.S. substrate as a function of cycle number during multiple deposition processes.*

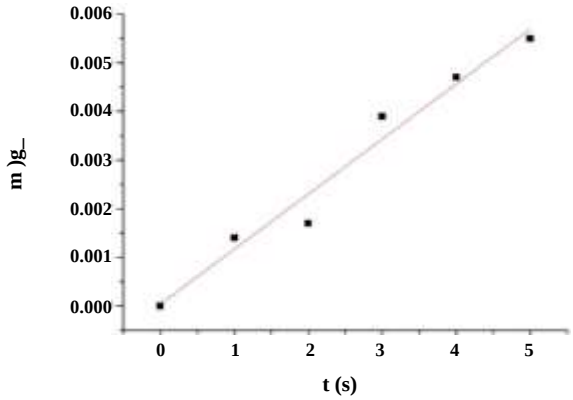


*Fig. 9: The deposit weight of xonotlite as a function of the deposition time.*

When the distance between electrodes is less, the effect of the electric field which occurs between them is stronger and EPD is more efficient.

Fig. 9 presents the dependence of the weight of the deposited xonotlite per surface area of the substrate of stainless steel in the function of the deposition time. As can be seen, the deposit weight of xonotlite increases almost linearly as the duration of the process increases.

Fig. 10 presents comparative morphological characteristics of the stainless steel substrate (S.S. substrate), electrochemically etched S.S. substrate, final coating of xonotlite in its native form, and after calcination at 900 ˚C. The micrograph in Fig. 10a shows that the S.S. substrate has a nonuniform and scraped surface which was polished by controlled corrosion of a metallic surface through electrochemical etching (Fig. 10b). Small-scale roughness can be observed on an etched surface providing a good basis for EPD coatings. After three repeated cycles of EPD, a very smooth and homogeneous surface of xonotlite coating with no visible cracks was obtained (Fig. 10c).

According to the measurement performed with a digital microscope Motic D-EL1, the xonotlite coating showed a thickness of 54 μm (Fig. 11).

After calcination (Fig. 10d) deposited layers show discrete cracks of almost uniform length which is usually having in mind that during drying and heat treatment, the coating undergoes a crystal phase transformation and densifies, and as a result, shrinks, but the substrate typically does not change dimension significantly. During this process, the coating will develop tensile stress it and these stresses will be relieved by the formation of cracks.

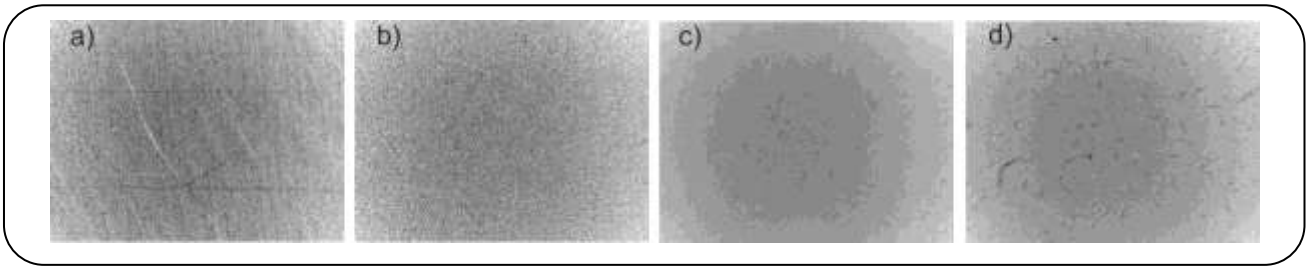


***Fig. 10: The micrograph of a) S.S. substrate, b) electrochemically etched S.S. substrate, c) xonotlite coating surface electrophoretically deposited on 304 S.S. substrate, and d) coated specimen calcined at 900 °C.***

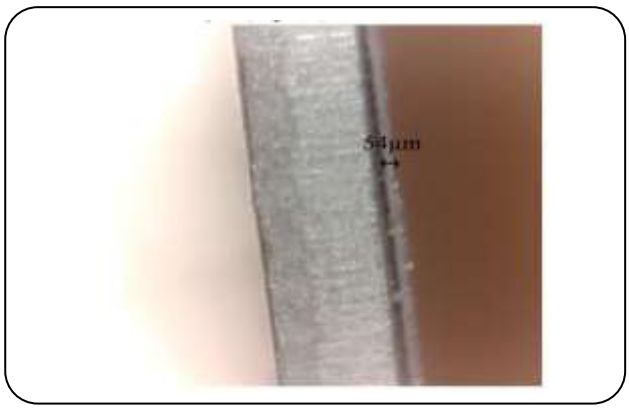


***Fig. 11: The coating thickness of xonotlite (54 μm) onto stainless steel substrates.***

## CONCLUSIONS

Xonotlite was synthesized by hydrothermal method and characterized by powder XRD and SEM. A small amount of wollastonite phase (up to 3%) was detected in the prepared product. After annealing at 900 ˚C pure wollastonite was produced as the final stable phase. The line broadening of xonotlite and wollastonite due to small crystallite size and the strain was analyzed by Scherrer's formula and Williamson and Hall's method. SEM images of xonotlite showed that it has a needle-like shape of particles in which random aggregation forms downy dendritic morphology. Xonotlite is very well-dispersed in a mixture of isopropanol-water (99:1) in the presence of $Ca^{2+}$ from which it can be electrophoretically deposited on a conductive substrate such as stainless steel. The resulting coating was smooth and crack-free upon drying at room temperature. After annealing at 900 °C it leads to the appearance of small cracks but the adhesion strength of the coatings to the substrate is improved.

**Acknowledgments**

The authors would like to acknowledge financial support from the Ministry of Education, Science and Technological Development of the Republic of Serbia (Agreement No 451-03-68/2020-14/200124)

*Received : Jul. 19, 2021 ; Accepted : Nov. 8, 2021*

## REFERENCES

[1] Mamedov K.S., Belov N.V., Structure of Xonotlite $Ca_6Si_6O_{17}(OH)_2$, *Dokl. Akad. Nauk SSSR*, **104**: 615-618 (1955).

[2] Mamedov K.S., Belov N.V., Crystal Structure of the Minerals of the Wollastonite Group. I. Structure of Xonotlite, *Zapiski Vserossiiskogo Mineralogicheskogo Obshcesteva*, **85**: 13-38 (1956).

[3] Black L., Garbev K., Stumm A., Structure, Bonding and Morphology of Hydrothermally Synthesised Xonotlite, *Adv. Appl. Ceram.*, **108(3)**: 137-144 (2009).

[4] Chen X., Kong H, Wu D., Wang X., Lin Y., Phosphate Removal and Recovery Through Crystallization of Hydroxyapatite Using Xonotlite as Seed Crystal, *J. Environ. Sci.*, **21**: 575–580 (2009).

[5] Mitsuda T., *Gypsum & Lime*, **229**: 464 (1990).

[6] Mitsuda T., *Gypsum & Lime*, **214**: 129 (1988).

[7] Cao J., Liu F., Lin Q., Zhang Y., Hydrothermal Synthesis of Xonotlite from Carbide Slag, *Prog. Nat. Sci.*, **18(9)**: 1147-1153 (2008).

[8] Oguar E., Botti R., Bortolotti M., Colombo P., Vakifahmetoglu C., Synthesis and Additive Manufacturing of Calcium Silicate Hydrate Scaffolds, *J. Mater. Res. Techn.*, **11**: 1142-1151 (2021).

[9] Konuklu Y., Ersoy O., Fabrication and Characterization of Form-Stable Phase Change Material/Xonotlite Microcomposites, *Sol. Energ. Mater.*, ***168:*** 130-135 (2017).

[10] Ohtsuki C., Kokubo T., Yamamuro T., Mechanism of Apatite Formation on $CaO\text{-}SiO_2$ $P_2O_5$ Glasses in a Simulated Body Fluid, *J. Non-Cryst. Solids*, **143**: 84-92 (1992).

[11] Salinas A.J., Vallet-Regi M., Izquierdo-Barba I., Biomimetic Apatite Deposition on Calcium Silicate Gel Glasses, *J. Sol-Gel Sci. Techn.*, **21(1)**: 13-25 (2001).

[12] Siriphannon P., Hayashi S., Yasumori A., Okada K., Preparation and Sintering of $CaSiO_3$ from Coprecipitated Powder Using NaOH as Precipitant And its Apatite Formation in Simulated Body Fluid Solution, *J. Mater. Res.*, **14(2)**: 529-536 (1999).

[13] Gou Z.R., Chang J., Synthesis and i*n vitro* Bioactivity of Dicalcium Silicate Powders, *J. Eur. Ceram. Soc.*, **24**: 93-99 (2004).

[14] Gou Z.R., Chang J., Gao J.H., Wang Z., In vitro Bioactivity and Dissolution of $Ca_2(SiO_3)(OH)_2$ and Beta-Ca2SiO4 Fibers, *J. Eur. Ceram. Soc.*, **24**: 3491-3497 (2004).

[15] Sarkar P., Nicholson S.P., Electrophoretic Deposition (EPD): Mechanisms, Kinetics and Application to Ceramics, *J. Am. Ceram. Soc.*, **79(8)**: 1987-2002 (1996).

[16] Chen X., Nouri A., Li Y., Lin J., Hodgson P.D., Wen C., Effect of Surface Roughness of Ti, Zr and TiZr on Apatite Precipitation from Simulated Body Fluid, *Biotechnol. Bioeng.*, **101(2)**: 378–387 (2008).

[17] Kokubo T., Surface Chemistry of Bioactive Glass-Ceramics, *J. Non-Cryst. Solids*, **120**: 138-151 (1990).

[18] Li P., Ducheyne P., Quasi-Biological Apatite Film Induced by Titanium in a Simulated Body Fluid, *J. Biomed. Mater. Res.*, **41(3)**: 341–348 (1998).

[19] Kokubo T., Kushitani H., Sakka S., Kitsugi T., Yamamuro T., Solutions Able to Reproduce *in vivo* Surface-Structure Changes in Bioactive Glass-Ceramics A-W, *J. Biomed. Mater. Res.* **24(6)**: 721-734 (1990).

[20] Shunmuga Sundaram P., Sangeetha T., Rajakarthihan S., Vijayalaksmi R., Elangovan A., Arivazhagan G., XRD Structural Studies on Cobalt Doped Zinc Oxide Nanoparticles Synthesized by Coprecipitation Method: Williamson-Hall and Size-Strain Plot Approaches, *Physica B*, **595**: 412342 (2020).

[21] Ferhat D., Nibou D., Mekatel E., Amokrane S., Adsorption of $Ni^{2+}$ Ions onto NaX and NaY Zeolites: Equilibrium, Kinetic, Intra Crystalline Diffusion and Thermodynamics Studies, *Iran. J. Chem. Chem. Eng. (IJCCE)*, **38(6)**: 63-81 (2019).

[22] Ouassel S., Chegrouche S., Nibou D., Melikchi R., Aknoun A., Mellah A., Application of Response Surface Methodology for Uranium(VI) Adsorption Using Hydroxyapatite Prepared from Eggshells Waste Material: Study of Influencing Factors and Mechanism, *Water Sci. Technol.*, **83(5)**: 1198–1216 (2021).

[23] Dowty E., Vibrational Interactions of Tetrahedra in Silicate Glasses and Crystals: I. Calculations on Ideal Silicate – Aluminate- Germanate Structural Units, *Phys. Chem. Miner.* **14**: 80-93 (1987).

[24] Frost R.L., Mahendran M., Pologanathan K., Xi Y., Raman Spectroscopic Study of the Mineral Xonotlite $Ca_6Si_6O_{17}(OH)_2$ – A Component of Plaster Boards, *Mater. Res. Bulletin*, **47**: 3644-3649 (2012).

[25] Frost R.L., López A., Xi Y., Scholz R., A Vibrational Spectroscopic Study of the Silicate Mineral Inesite $Ca_2(Mn, Fe)_7Si_{10}O_{28}(OH)\cdot 5H_2O$, *Spectrochimica Acta Part A: Molecular and Biomolecular Spectroscopy*, **128**: 207-211 (2014).

[26] Frost R.L., López A., Scholz R., Theiss F.L., Romano A.W., SEM, EDX, Infrared and Raman Spectroscopic Characterization of the Silicate Mineral Yuksporite, *Spectrochim. Acta A*, **137**: 607-611 (2015).

[27] Nibou D., Amokrane S., Mechanism of $Cu^{2+}$ Ions Uptake Process by Synthetic Naa Zeolite from Aqueous Solution: Characterization, Kinetic, Intra-Crystalline Diffusion And Thermodynamic Studies, *J. Mol. Liquids*, **323**:114642 (2021).

[28] Mostafa Y., Shaltout A.A., Omar H., Abo-El-Enein S.A., Hydrothermal Synthesis And Characterization of Aluminium And Sulfate Substituted 1.1 nm Tobermorites, *J. Alloy. Compd.*, **467**: 332–337 (2009).

[29] Wang S., Peng X., Tang L., Zeng L., Lan C., Influence of Inorganic Admixtures on the 11 Å-Tobermorite Formation Prepared from Steel Slags: XRD and FTIR Analysis, *Constr. Build. Mater.* **60**: 42-47 (2014).

[30] Pantoja-Pertegal J.L., Díaz-Parralejo A., Macías-García A., Sánchez-González J., Cuerda-Correa E.M., Design, Preparation, and Characterization of Yttria-Stabilized Zirconia (YSZ) Coatings Obtained by Electrophoretic Deposition (EPD), *Ceram. Int.*, **47(10)**: 13312-13321 (2021).